# PROPER ORTHOGONAL DECOMPOSITION ANALYSIS ON CYCLE-TO-CYCLE VARIABILITY OF HIGH-PRESSURE GASOLINE SPRAYS FOR INTERNAL COMBUSTION ENGINES

A Thesis

Presented to

The Faculty of the Department of Mechanical Engineering

California State University, Los Angeles

In Partial Fulfillment

of the Requirements for the Degree

Master of Science

in

Mechanical Engineering

By

Blakeley Ficenec Williams

August 2023

© 2023

Blakeley Ficenec Williams

ALL RIGHTS RESERVED

The thesis of Blakeley Ficenec Williams is approved.

Mario Medina, PhD, Committee Chair

Jim Kuo, PhD

Arturo Pacheco-Vega, PhD

David Raymond, PhD, Department Chair

California State University, Los Angeles

August 2023

ABSTRACT

Proper Orthogonal Decomposition Analysis on Cycle-to-cycle Variability of High-pressure Gasoline Sprays for Internal Combustion Engines

By

Blakeley Ficenec Williams

Data analytics has grown in recent years and a commonly used technique is called model reduction, which helps reduce high-dimensional dynamics into low dimensions. Model order reduction is a general category of techniques, which include proper orthogonal decomposition or POD. Generally, POD decomposes a physical field like turbulent fluid flows or vibrations from structures and extracts “mode shapes” or basis functions from experimental data to yield low-dimensional dynamic models [1]. The basis functions represent the dominant or coherent structures from a given scalar fields set [2]. POD methods like balanced truncation, minimize the difference between the basis function and the data set, however, it is not as sensitive to detail like POD and becomes computationally intractable for very large dimensions (> 10,000 states) [3].

This research consisted of applying the snapshot POD method on fuel injector spray data, characterizing coherent structures, and quantifying the variability exhibited in the spray images between operating conditions. This POD method was chosen because of its ability to handle images and the capacity to eliminate statistical noise from the data. The data consists of high-pressure gasoline sprays injected inside a constant volume chamber at various operating conditions, i.e., injection pressures of 300 – 1500 bar and chamber pressures of 1 – 20 bar. Results contain information on cycle-to-cycle variability between

injection events. The cycle-to-cycle variability allowed for quantitative differences in the spray patterns and intensity in the variations.

TABLE OF CONTENTS

Abstract ..... iv

List of Tables ..... viii

List of Figures ..... ix

Chapter

1. Introduction ..... 1

1.1 Background ..... 1

1.2 Visual Comparison of POD Methods ..... 3

1.3 Snapshot POD ..... 6

1.4 Motivation, Research Objectives, and Thesis Contents ..... 8

1.5 Fuel Injectors and Experimental Setup ..... 10

2. Specifics of the Math ..... 14

2.1 Methods and Equations ..... 14

2.1.1 Eigenvalue Problem ..... 16

2.1.2 SVD with Correlation Matrix ..... 17

2.1.3 Economy-size SVD without Correlation Matrix ..... 18

2.2 Examples ..... 18

2.3 Discussion ..... 24

3. Data Analysis and Interpretation ..... 28

3.1 Cycle-to-cycle Variability ..... 28

3.1.1 Injection Pressures of 600 bar ..... 28

3.1.2 Chamber Pressures of 1 bar ..... 33

3.1.3 Injection Pressures of 1500 bar ..... 35

3.1.4 Mode 1 vs. Time for Injection Pressures of 600 bar.....37

3.1.5 Mode 1 vs. Time for Chamber Pressures of 1 bar .....38

3.1.6 Mode 1 vs. Time for Injection Pressures of 1500 bar.....39

3.2 Discussion.....40

4. Conclusions and Recommendations for Future Work.....42

4.1 Conclusions.....42

4.2 Recommendations for Future Work.....44

References.....45

LIST OF TABLES

Table

1.1 Experimental Conditions .....11

1.2 Camera Conditions.....11

1.3 Fuel Properties .....12

LIST OF FIGURES

Figure

1.1 Mode 1 for POD Methods....4

1.2 Mode 2 for POD Methods....4

1.3 Mode 3 for POD Methods....5

2.1 SVD Representation....17

2.2 Temporal Evaluation of Raw Spray Data for Injection Pressure of 600 bar and Chamber Pressure of 20 bar....19

2.3 Energy Fraction for Eigenvalue Problem....21

2.4 Energy Fraction for SVD with Correlation Matrix....22

2.5 Energy Fraction for SVD with Economy-size Decomposition....23

2.6 Combined Energy Fraction Graph....25

3.1 Energy Fractions for Injection Pressures of 600 bar for Time Frame 30....29

3.2 Modes of 600 bar & 1 bar and 20 bar for Time Frame 30....30

3.3 Coefficients of Mode 1 for Condition 600 bar &1 bar....31

3.4 Coefficients of Mode 1 for Condition 600 bar & 20 bar....32

3.5 Energy Fractions for Chamber Pressures of 1 bar for Time Frame 30....33

3.6 First Mode of 600 bar, 900 bar, and 1500 bar and 1 bar for Time Frame 30....34

3.7 Energy Fractions for Injection Pressures of 1500 bar for Time Frame 30....36

3.8 First Mode of 1500 bar & 1 bar and 20 bar....37

3.9 Mode 1 vs. Time for Injection Pressure of 600 bar....38

3.10 Mode 1 vs. Time for Chamber Pressure of 1 bar....39

3.11 Mode 1 vs. Time for Injection Pressure of 1500 bar....40

# CHAPTER 1

# Introduction

## Background

The field of data analysis has grown significantly in the past several years with advancements in new technologies and increased data generation. Facial recognition in cell phones, autonomous/assisted driving, chatGPT, neural networks are examples of data driven tools [4]. While these technologies generate/use large datasets, there remains a challenge to increase interpretability while preserving the most amount of information. Principal component analysis (PCA) is a widely used statistical tool for dimensionality reduction while also facilitating visualization of multidimensional data. PCA remains the most well-known, but there are similar methods such as proper orthogonal decomposition (POD), factor analysis, and singular value decomposition (SVD) that were introduced in different fields by different people, all with an intent of dimensionality reduction. POD was first developed by Lumley in 1967 and was applied to turbulent flows to analyze coherent structures [5]. Since its first use, POD has been applied to a wide range of fluid flows including in-cylinder engine flows [5] [6], cycle-to-cycle variability (CCV) [2] [7] and turbulent gaseous and liquid jets [8] [9]. The POD method provides a generic, analytic tool that can be used efficiently [10]. In this method there exists an optimal basis in which a given system can be written so that in this basis, all redundancies have been removed, and the largest variances of measurements are ordered and written in terms of its principal components [10]. Like POD, SVD can also be used as a method for data reduction. SVD is a method for identifying and ordering dimensions along which data points exhibit the most variation [11]. Once identification is made on where the most variation is, it is then

possible to find the best approximation of the original data points using fewer dimensions [11]. Ultimately, SVD takes a high dimensional, highly variable set of data points and reduces it to a lower dimensional space that exposes the substructure of the original data more clearly and orders it from most variation to the least [11].

Varying applications have required various developments of POD throughout the years. Some of the most common are balanced truncation, balanced POD, and snapshot POD. Each method provides slight advantages over others and will be briefly described here. Balanced truncation was first introduced by Moore for control theory of stable, linear input-output systems [12]. This method is notable for minimal error bounds compared with other reduced order models including PCA [3]. Additionally, balanced truncation has been applied to nonlinear fluid systems. However, such flows become computationally intractable given the large number of dimensions (>10,000 states) [3]. Primarily, the technique is unsuitable for turbulent flows, but works well in balanced linear systems, since these systems allow for the number of equations and variables to balance and create an algebraic solution. Balanced POD combines the attractive qualities of POD and balanced truncation. It obtains an approximation to balanced truncation by minimizing the error bounds to the lowest error possible from any reduced-order model, which is computationally tractable for large systems [3]. POD computes a set of linearly independent basis vectors indirectly allowing for large datasets [3]. The major limitation of balanced POD is applicability for stable and linear systems. Several studies highlight this method including Moore and Lall et al. [12] [13]. Lastly, snapshot POD advantageously computes the set of linearly independent basis vectors directly using singular value decomposition (SVD) of an $n \; x \; n$ data matrix [3]. Similarly, a direct solution

can be computed from the eigenvalue problem if the systems contain less than $10^6$ dimensions [3]. This method also separates time away from the data allowing for more simplicity of the snapshot POD and making it an attractive technique for turbulent flow problems.

**Visual Comparison of POD Methods**

The three POD methods described above have been analyzed and compared by Rowley et al. [3]. The POD modes are calculated to be the eigenvectors and the columns of the $n \; x \; m$ matrix. This is done for each method that was discussed in section 1.1 above. Balanced truncation is able to provide better reduced-order models whereas balanced POD is a more tractable method for computing approximate balanced truncations, and snapshot POD decomposes a data set into a linear combination of orthonormal basis with corresponding coefficients. A visual representation of the first three modes for each method is shared below in Figures 1.1 – 1.3 [3]. The analysis was applied using balanced truncation, balanced POD, and snapshot POD (called POD). All three figures represent a fluid flow example where the flow runs parallel within a plane channel.

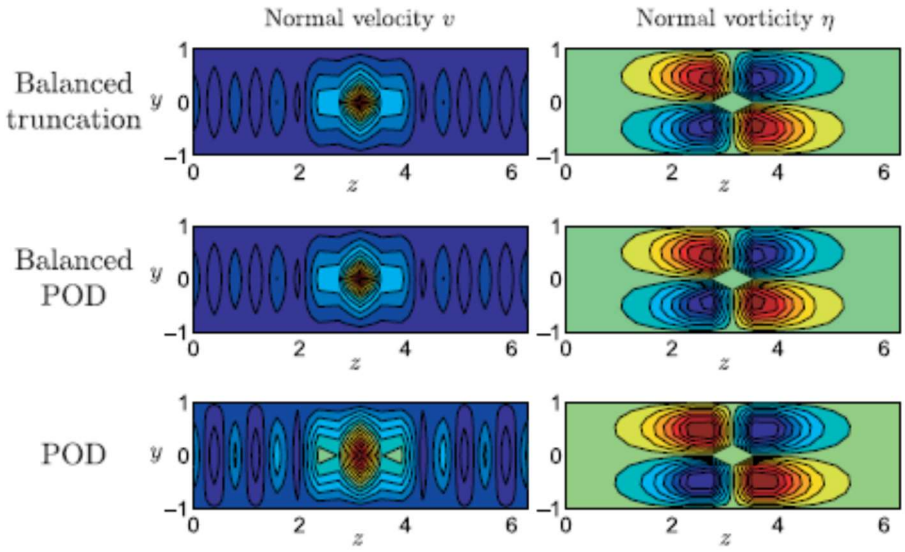



Figure 1.1 – Mode 1 for POD Methods [3]

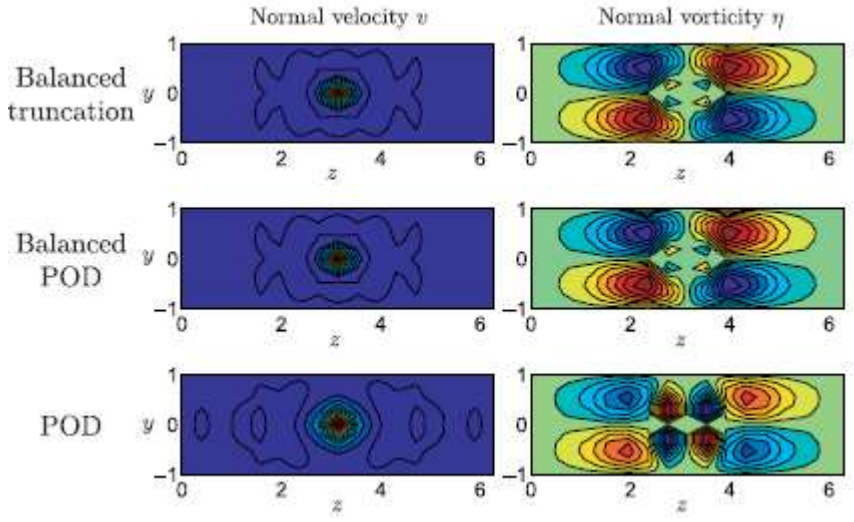



Figure 1.2 – Mode 2 for POD Methods [3]

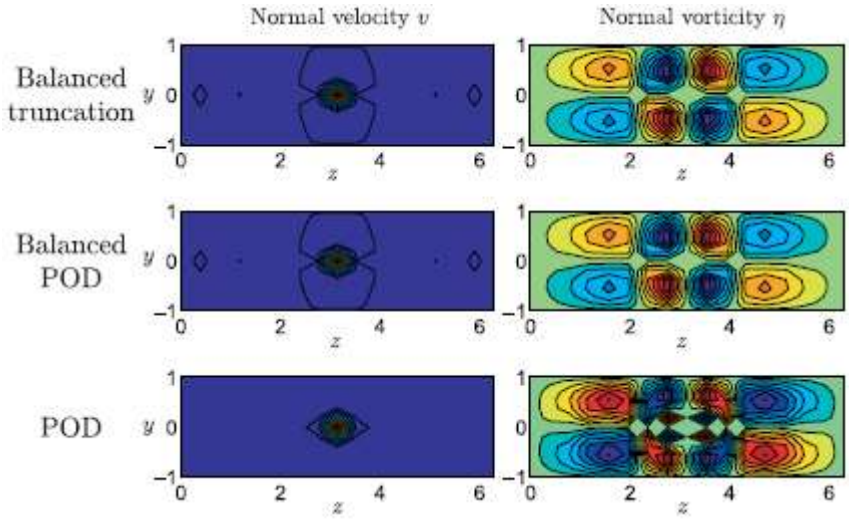



Figure 1.3 – Mode 3 for POD Methods [3]

The analysis decomposes the data in order of strength such that mode 1 contains the strongest features shared in each velocity and vorticity field. Such is the case in Figure 1.1, the velocity field is highest in the first mode and begins to decrease in the second and third modes. The vorticity is interpreted the same as the velocity, where it is the highest in the first mode for each method. By mode 3, the vorticity has split as the rotations in the channel flow have decreased. In Chapter 2 and 3, similar findings are shown with the spray images that are being analyzed under this research and conclusions are made about the first mode describing the highest spatial differences between the spray cycles.

Under the snapshot POD method, the modes look relatively the same for the general structure, especially for the first mode, but there are great differences for the second and third modes [3].

The comparison of these figures helps to confirm findings from other researchers where the first mode provides the most dominant pattern in the data set, the second mode represents the secondary dominant pattern in the data, and so on [6].

**Snapshot POD**

The foundational concept of POD is to decompose a data set into a linear combination of orthonormal basis with corresponding coefficients. For a 2-D data set, the basis functions are representative unit vectors that minimize the Euclidean error, distance between two points, and the coefficients are scalar transformations. These basis functions are often called "modes" and they contain dominant features or representative trends within the data. For liquid jets, this may be vortex structures, cycle-to-cycle variability, cavitating flows, or other flow patterns [14]. Specifically, the snapshot POD method has been commonly applied to discretized data that is repeatable and develops temporally and spatially. The snapshot POD was originally introduced by Sirovich in the 1980's [15]. In the context of this thesis, the data set is the temporal and spatial development of a liquid spray for various operating conditions (i.e., injection pressure and chamber pressures).

The mathematical representation of snapshot POD is as follows. For an experiment imaged K times, each image is a scalar field represented by $S^{(k)}$. The image S is a matrix of size $I\ x\ J$ pixels. The entire data set is represented as a matrix of size $I\ x\ J\ x\ K$. The POD decomposes the input data set into a linear combination of $K$ spatial basis functions, $\phi$, and their corresponding coefficients $c_i^{(k)}$:

$$S^{(k)} = \sum_{i=1}^{K} c_i^{(k)} \phi_i \qquad (1.1)$$

The POD "modes" or spatial basis functions describe the coherent structures of the data set $S^{(k)}$ and the coefficients represents the strength or dominance of what the ith mode has for the kth snapshot [7]. In vector notation, the modes are the vectors, and the

coefficients are the amplitudes to recover the kth image. The decomposition presents the coefficients and modes in decreasing order, such that the first mode describes the strongest features shared in all images, S, followed by the second mode which represents the second most dominant features and so on, with the kth mode capturing statistical noise. Under certain applications, the first mode describes the average behavior of the entire data set, $S^{(k)}$, while the second mode represents the most shared dominant features, i.e., a vortex structure, directionality, distance, or variability.

The snapshot POD can be calculated with different approaches. Weiss [5] provides a detailed description of POD and discusses three algorithms for calculating the decomposition of a turbulent separation-bubble flow. The study does not provide visual comparisons between methods, but instead refers to the data in abstract form. In fact, many studies use slightly different methods with limited comparisons [6] [2] [1]. Given the numerous POD and PCA techniques mentioned, there is a need to understand the fundamental differences between techniques. Thus, metrics for comparison must first be discussed.

The results of the decomposition have been commonly interpreted using similar metrics even when different methods are applied. These include the energy fraction, the modes, and their coefficients. The energy fraction explains the energy distribution between the modes. With repeatable data, the vectors of the images form a cluster and point in the same direction, concentrating most of the energy in the first few modes. On the other hand, large variation within a data set will translate into a larger length of space. More energy will be distributed throughout the modes.

The modes that are observed in the images of the sprays are compared for each mode. The modes are a measure of how the velocity is correlated at different points in the flow [5]. A zone of correlation can represent a coherent structure when the corresponding energy is dominant compared to the other modes [5]. There are many POD modes that add up to complete the flow when multiplied by their time coefficients and some of these zones of correlation appear randomly often due to the turbulent nature of most practical flows, meaning that these modes are a manifestation of the randomness of turbulence [5].

**Motivation, Research Objectives, and Thesis Contents**

Free shear flows serve as a great canvas to study turbulent structures, cycle-to-cycle variability, cavitation-induced variability and forced variability induced by experimental conditions. Additionally, the results of a POD analysis can inform turbulence models to improve modeling and prediction. Liquid jets are a free shear flow where atomization and entrainment are important physical processes that govern a wide range of applications including power generation, emissions control, agriculture, and manufacturing. Fuel injection for internal combustion engines serve a crucial role in performance and emissions and are subjugated to the physics mentioned above.

The objective of the present work is to contribute to the existing research on POD by taking data in the form of raw spray images from a high-pressure liquid fuel spray for an internal combustion engine and characterize the coherent structures and quantify the variability. The data is in the form of high-speed images (> 50,000 fps) recorded using diffuse back-lit shadowgraph in a constant volume chamber (CVC). The idea is to research and evaluate different approaches to snapshot POD and find ways to compare them quantitatively. These approaches are the eigenvalue problem, SVD with a correlation

matrix, and SVD using the economy size decomposition. Variability is studied between repetitions of the same condition i.e., cycle-to-cycle variability, and among different operating conditions i.e., injection pressure and chamber pressure. The present work focuses on a POD analysis for experimental data that was previously collected. The full details of the experimental matrix are provided in Medina et al. [16] [17] and briefly summarized in the next section.

Chapter 2 presents the technical approach of the POD analysis. Firstly, the fundamental linear algebra is discussed in the context of images. From constructing the data matrix to defining the decomposition and its outcomes. Also introduced is a qualitative analysis of the "modes". Given the vast applicability and numerous techniques, discussing the differences between a handful of POD techniques was necessary. Specifically, the "snapshot" method is solved using three techniques: using the eigenvalue problem, using SVD with a correlation matrix, and using SVD with an economy-size decomposition. The results are presented as energy fractions and are the primary metrics for comparison for each technique.

Chapter 3 presents the results of the snapshot POD technique solved by using SVD with an economy-size decomposition applied to the entire experimental matrix discussed in section 1.5. A qualitative analysis is discussed for POD modes to identify coherent structures and cycle-to-cycle variability for the extreme conditions in the experimental matrix. A quantitative analysis is presented to identify mechanisms of cycle-to-cycle variability and forced variability induced by experimental conditions. Energy fractions and qualitative analyzations of the modes are compared for experimental conditions.

The final chapter summarizes the key conclusions of each chapter and provides recommendations for future work.

**Fuel Injectors and Experimental Setup**

Portions of the following section appear in the technical papers written by Dr. Medina and referenced under [16] [17].

Fuel injectors are the devices that are used to force and atomize fuel straight into internal combustion engines. The experiment that gathered the raw data utilized three different fuel injectors. Injector 1 is a single hole injector and injectors 2 and 3 are both double hole injectors. A summary of the experimental conditions is shown in Table 1.1. The spray development was examined by diffusing backlit shadowgraph imaging and the setup consisted of a constant volume chamber with an internal spherical diameter of 12.4 cm. The chamber used for this experiment was equipped with three optical access ports, of which only two were utilized, and others for instrumentation and measurement. The optical access ports that were used are those perpendicular to the axis of the injector, each having a viewing diameter of 7.6cm. One of the ports was to allow for the diffusion of light to illuminate the chamber and the other was used for imaging.

The chamber had a maximum chamber pressure of 100 bar and was pressurized with the use of an ultra-high purity grade nitrogen, PurityPlus Gases with a purity rating of 99.999%. The Supco-DPG1000 pressure gauge was used to observe the chamber pressure and a K-type thermocouple was used to monitor the chamber temperature. The range of chamber pressures used in the study was 1 to 20 bar with a repeatability of ± 0.2 bar at a temperature of 298 K.

Table 1.1 – Experimental Conditions

| | |
|---|---|
| Chamber gas | Nitrogen |
| Fuel type | Reference grade gasoline |
| Injector 1 type | Single hole, centered |
| Injector 2 type | Double hole |
| Injector 3 type | Double hole |
| Injector 1 hole size (µm) | 110 |
| Injector 2 hole size 1 & 2 (µm) | 109.8; 190 |
| Injector 3 hole size 1 & 2 (µm) | 149.9; 149.9 |
| Injection duration (ms) | 1 |
| Injection pressure (bar) | 300, 600, 900, 1200, 1500 |
| Chamber temperature (K) | 298 |
| Chamber pressure (bar) (chamber density ($kg/m^3$) at 298K) | 1 (1.133), 5 (5.65), 10 (11.33), 20 (22.66) |

The Vision Research Phantom v7.11 12-bit CMOS array was the high-speed camera used to capture the injection events under this experiment. Over the course of the experiment, there were two data sets recorded: near-nozzle images and bulk spray images. Those used under this research are the sets of bulk spray images. The camera settings are all listed in Table 1.2. The lenses that were utilized for both data sets were a Nikon Nikkor 105 mm lens.

Table 1.2 – Camera Conditions

| **Setting** | **Macro Spray Imaging** |
|---|---|
| Frame rate (fps) | 69,000 |
| Exposure time (µm) | 14 |
| Lens aperture (f/#) | 5.6 |
| Camera resolution (pixel x pixel) | 608 x 152 |
| Image resolution (pixels/mm) | 13.9 |

The fuel type that was used for this experiment is a reference grade gasoline from Gage Products Co., product number 40665-55F, and the fuel properties are in Table 1.3.

Table 1.3 – Fuel Properties*

| Property | Test Method | Value |
|---|---|---|
| Fuel Type | - | Reference grade gasoline, 40665-55F |
| Specific gravity 289 K | ASTM D4052 | 0.743 |
| Reid vapor pressure (kPa) | ASTM D5191 | 61.46 |
| Research octane number | ASTM D2699 | 91.5 |
| Motor octane number | ASTM D2700 | 83.4 |
| Heat of combustion (MJ/kg) | ASTM D240 | 43.6 |
| H/C ratio (Mole basis) | Gage-calculated | 1.91 |
| Distillation, IBP (K) | ASTM D86 | 305.2 |
| Distillation, 10% (K) | ASTM D86 | 322.9 |
| Distillation, 50% (K) | ASTM D86 | 372.4 |
| Distillation, 90% | ASTM D86 | 428.2 |

*As per manufacturer specifications.

For the purposes of the experiment, the fuel was blended with 350 ppm by volume of lubricity additive (Infineum R655) to allow operation with the diesel pump and injection system. The fuel pressure range was 300 to 1500 bar. The injectors used for this experiment were prototype research-grade injectors developed by Bosch. The injector bodies were production diesel hardware, and the nozzles were custom designed with canonical internal architectures to study specific geometric features. Injector 1 has one hole centrally located with a converging nozzle and a high percentage of hydro-erosion rounding of the nozzle inlet. Hydro-erosion increases the statis flow rate by rounding the nozzle inlet edges. The percentage of hydro-erosion rounding reflects the percent increase in the static flow rate. Injector 2 and 3 both have two holes oriented on the same plane with 30° of separation and the holes are located 15° above and below the horizontal plane. Injector 2 had two nozzles with two different outlet diameters each with straight nozzle passages and no inlet rounding. Injector 3 had two nozzles, each with the same outlet diameter and each with hydro-erosion rounding of the nozzle inlet. However, one nozzle passageway was diverging and the other was converging. Nozzle passage conicity was measured relative to the nozzle exit diameter, where a straight or uniform passageway had a conicity of 0, a

converging nozzle had a positive conicity, and a diverging nozzle had a negative conicity. The injectors were all controlled electronically using a LabView based program with 1 ms injection events. Labview was also programmed to synchronize the injection events with the camera trigger.

The experiment that gathered all the raw data that is used in this research was completed prior to the onset of the research and is not part of the analysis.

CHAPTER 2

Specifics of the Math

**Methods and Equations**

In this section the fundamental elements of the snapshot POD are discussed. The decomposition was performed using the eigenvalue problem, SVD with a correlation matrix, and SVD with "economy-size" decomposition. The general structure is specified here and remains the same for all approaches. The outcomes of each approach are described in their respective sections.

Suppose a repeatable, discrete scalar field is represented as a matrix with size - $I\ x\ J\ x\ K$, where $I\ x\ J$ represent the scalar field and $K$ represents the number of repetitions. The data matrix can be restructured such that each field is stacked into one row (L) and the number of rows indicate the number of repetitions, K, as shown in Equation 2.1:

$$S = \begin{bmatrix} S^{(1)} \\ S^{(2)} \\ \vdots \\ S^{(K)} \end{bmatrix} = \begin{bmatrix} s^{(1)}_{i=1,j=1} & s^{(1)}_{i=1,j=2} & \cdots & s^{(1)}_{i=1,j=J} & s^{(1)}_{i=2,j=1} & \cdots & s^{(1)}_{i=I,j=J} \\ s^{(2)}_{i=1,j=1} & s^{(2)}_{i=1,j=2} & \cdots & s^{(2)}_{i=1,j=J} & s^{(2)}_{i=2,j=1} & \cdots & s^{(2)}_{i=I,j=J} \\ \cdots & \cdots & \cdots & \cdots & \cdots & \cdots & \cdots \\ s^{(K)}_{i=1,j=1} & s^{(K)}_{i=1,j=2} & \cdots & s^{(K)}_{i=1,j=J} & s^{(K)}_{i=2,j=1} & \cdots & s^{(K)}_{i=I,j=J} \end{bmatrix} \quad (2.1)$$

The data matrix $S$ is an $L\ x\ K$ matrix where $L = I\ x\ J$. Velocity, temperature, and pressure fields are examples of such a scalar field. For images of turbulent flows, the light intensity captured by the camera sensor also serves as a discrete scalar field. These images can be decomposed into a linear combination as shown in Equation 2.2.

$$S = \sum_{i=1}^{K} c_i^{(k)} \phi_i \quad (2.2)$$

Where $c_i^{(k)}$ are the coefficients that represent the strength features of what an ith basis has on the k[th] image and $\phi$ represents the spatial basis functions of size $I\,x\,J$. The basis functions are obtained by minimizing the Euclidean error following Equation 2.3 [3] [7].

$$\sum_{k=1}^{K} \left\| S - \sum_{i=1}^{r} C_i^{(k)} \varphi_i \right\|^2 \rightarrow min \tag{2.3}$$

Where || || denotes the $L^2$ norm, and r < K for any subset of the $S$. The basis functions are normalized in the Euclidean space such that the sum of the squares of the vectors is unity. Each basis function is also orthogonal to all others, resulting in orthonormal basis functions. The basis functions contain "flow patterns" for every structure of every image, however the modes may not be physical coherent structures [18]. Since each structure is present in every basis function, the magnitude of the structure is represented by the coefficients. Suppose a repetition does not contain a structure present in the basis function, the coefficient that corresponds to that image will have a zero magnitude.

To determine the coefficients, the original matrix $S$ is projected onto the computed basis functions, $\phi$. Thus, each repetition can be reconstructed using Equation 2.2, summing all the modes with the respective coefficient for that repetition. The coefficients can also be used to understand how the energy is distributed between the modes. In other words, when most of the energy is concentrated in the first few modes, the repetitions can be considered consistent. The concept of "low-order modeling" arises from this result because only a few modes are necessary to capture a majority of the flow behavior. While more energy distributed throughout more modes signifies larger variation in the data. The energy fraction is calculated using Equation 2.4. It should be noted that the concept of energy does

not refer to a thermodynamic property when applied to a scalar field of light intensity, but rather "information" of the data set [1] [19].

$$E_m = \frac{1}{2}\sum_{i=1}^{K}\left(c_i^{(k)}\right)^2 \tag{2.4}$$

**Eigenvalue Problem**

The standard algebraic eigenvalue problem finds the eigenvectors and eigenvalues that satisfies Equation 2.5, where the eigenvectors are a nonzero vector and

$$Cx = \lambda x \tag{2.5}$$

$\lambda$ represents the eigenvalues, x represents the eigenvectors, and C represents a $n\ x\ n$ matrix. To solve the eigenvalue problem for an $n\ x\ m$ image, such as the data matrix $S$, the matrix requires truncation or modification. A spatial correlation matrix can be constructed using $S$ demonstrated by Equation 2.6.

$$C = \frac{1}{n-1}SS^T. \tag{2.6}$$

The correlation matrix is symmetric and thus restricts the eigenvectors from forming an orthonormal basis. Solving the eigenvalue problem results in ordered eigenvalues from largest to smallest and obtaining the eigenvectors requires a projection of the data matrix. Lastly, the spatial coefficients shown in Equation 2.2 are obtained by projecting the data matrix **S** onto the eigenvectors [5].

### SVD with Correlation Matrix

A more direct method of solving for the basis functions and their respective coefficients results from computing the SVD of the data matrix **S** as shown in Figure 2.1 below.

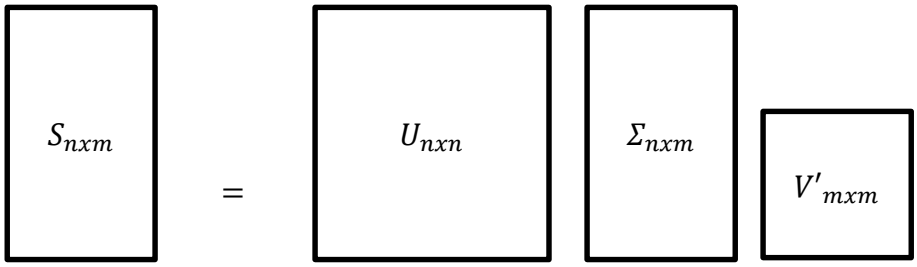



Figure 2.1 – SVD Representation

The decomposition results with orthonormal matrices, $U$ and $V$ and a diagonal matrix with decreasing and nonnegative diagonal entries, Σ. Conveniently, the columns of matrix $U$ are the POD modes while the coefficients are obtained by matrix multiplication of Σ and V. Secondly, the matrix, Σ, contains the singular values, $\sigma$, of $S$ which are associated with the eigenvalues ($\lambda = \sigma^2$). The eigenvalues in this case have the same meaning as the eigenvalue problem in the previous section. It should be noted that the decomposition is suitable for square matrices with lower dimensions.

SVD decomposes one complex transformation into simpler transformations of rotation and scaling. When focused on transformations, matrices $U$ and $V'$ cause the rotation and the diagonal matrix Σ causes the scaling. This ultimately allows for the original matrix to be displayed as a linear combination of low-rank matrices.

### Economy-size SVD without Correlation Matrix

Economy-size decomposition is computed using the SVD, but requires truncation when using a rectangular matrix, such as matrix $S$. Assuming $S$ is an $L\ x\ K$ matrix such that $L > K$, only the first $K$ eigenvectors are computed using this method.

Since this approach does not require that $L = K$, such as the correlation matrix C necessary in the previous approaches, the SVD does not require the data to be centered by the mean, normalized, or standardized resulting in a faster execution. The SVD approaches are more direct compared with the eigenvalue approach [5]. However, economy size SVD does not require additional processing. The advantage of the economy-size decomposition removes extra rows/columns of zeros from the diagonal matrix of singular values, Σ. A similar procedure is followed as described in the previous section.

### Examples

The three approaches that are described in the previous section have each been compared and evaluated under a single condition. The selected condition is an injection pressure of 600 bar and a chamber pressure of 20 bar (600 & 20). Each method uses the same set of images with the same start of injection (SOI). A montage evolution of the raw spray images is shown in Figure 2.2 below to help describe the progress in the x-direction as a function of time. The first image is the SOI followed by six other images varying with after start of injection (ASOI) time.

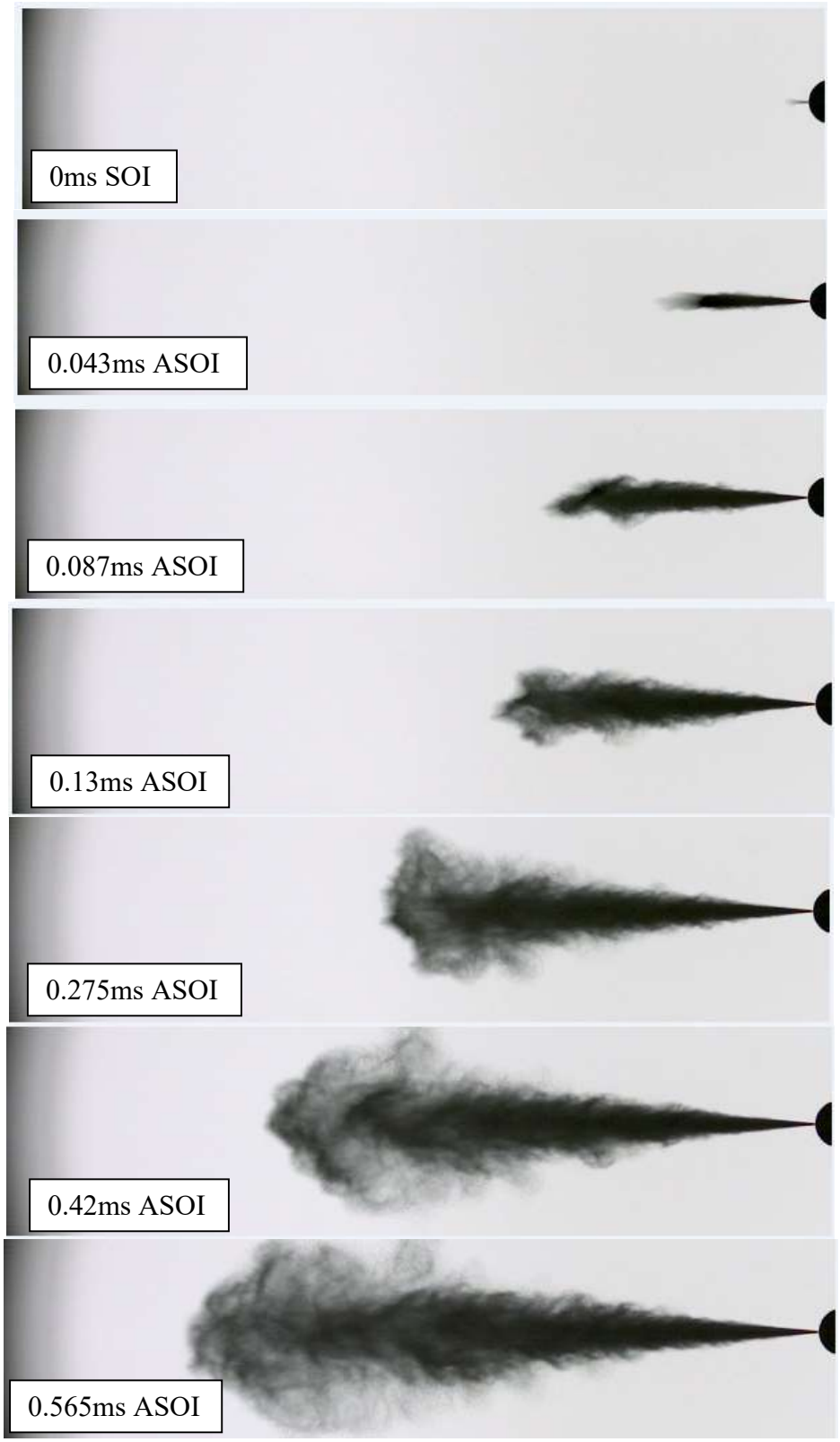


Figure 2.2 – Temporal evolution of raw spray data for injection pressure of 600 bar and chamber pressure of 20 bar

To understand the key differences across each approach of the snapshot method, POD needs to be related to the raw sets of spray-imaging data. The development begins with the use of a matrix as described in the previous section of the first frame ASOI of each set of images, applying the POD to that matrix, calculating the energy fraction for each one of the POD modes, and then repeating the steps for the next frame ASOI.

An example of a calculated energy fraction for the first 20 modes of time stamp 1, 2, and 30 of the 600 & 20 condition is shown in Figure 2.3. This graph is one of the key comparisons that is used across each approach. To be able to show high variability amongst each mode, the ensemble mean is subtracted from the data set. When the ensemble mean is subtracted, the first mode does not represent the average, however, it represents the most statistically large spatial differences between the cycles.

Figure 2.3 is from the eigenvalue problem approach describing the changes at each instant of time on how the energy is distributed. The changes depend on how steady or variable the spray distribution is at the time the snapshot is taken. In this approach, the ensemble mean was subtracted from the dataset, and so the first mode describes a higher energy fraction than the remaining modes, representing that the pattern of the spray is similar from one cycle to the next. Furthermore, this shows that there is a low amount of variability between each cycle and the first mode can capture majority of the ensemble behavior. If the first mode's energy fraction were to be lower, this would tell that the differences in the sets of spray data are more complicated.

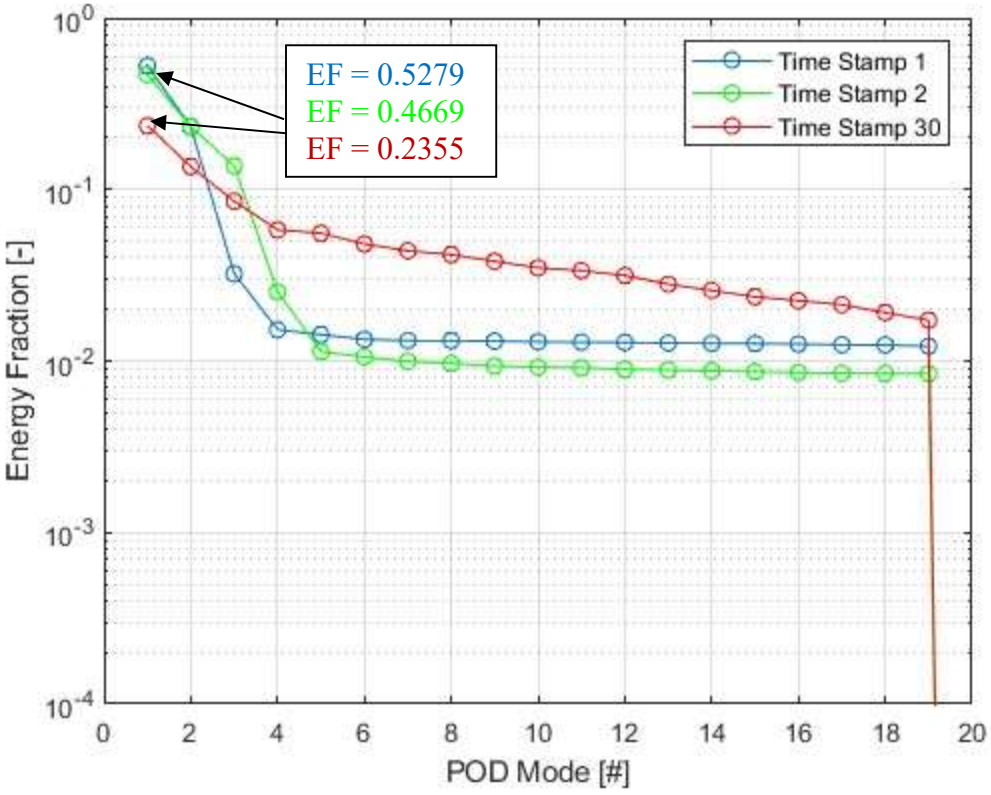



Figure 2.3 – Energy Fraction for Eigenvalue Problem

The same energy fraction is taken for the next approach, SVD with the use of a correlation matrix and this graph is displayed in Figure 2.4.

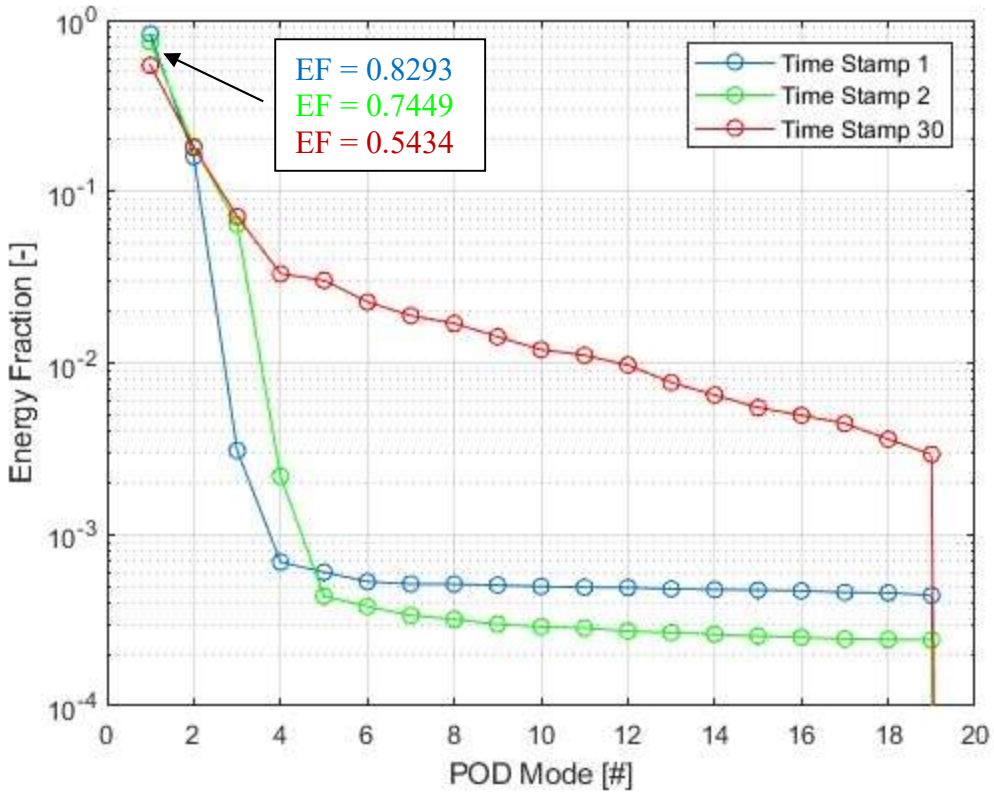



Figure 2.4 – Energy Fraction for SVD with Correlation Matrix

With this approach, this study found that the energy fraction of the first mode is also the highest for each time stamp. This approach also subtracts the ensemble mean from the data set, therefore, similarly telling that the first mode has a higher energy fraction than the remaining modes, indicating that the pattern of the spray is similar from one cycle to the next. Like the previous approach, the first mode has the highest energy fraction, which indicates that the pattern of the spray is consistent from one cycle to the next. Comparing the differences among these first two approaches it is noticed that each time stamp is different, especially the first and second. There is a significant drop for the third mode of time stamp one in Figure 2.4 compared to that of Figure 2.3. Time stamp one drops from an energy fraction of 0.8293 at mode one to an energy fraction of 0.0031 at mode three. In Figure 2.3 time stamp one drops from an energy fraction of 0.5279 at mode one to an

energy fraction of 0.0322 at mode three. SVD with the correlation matrix approach shows a similar trend as the eigenvalue problem, however, in magnitude the energy fractions are much larger by almost double. The third approach has an identical trend to the eigenvalue problem, therefore, also being a similar trend to the previously discussed approach. Figure 2.5 shows the energy fraction graph for the third approach that was assessed under this research.

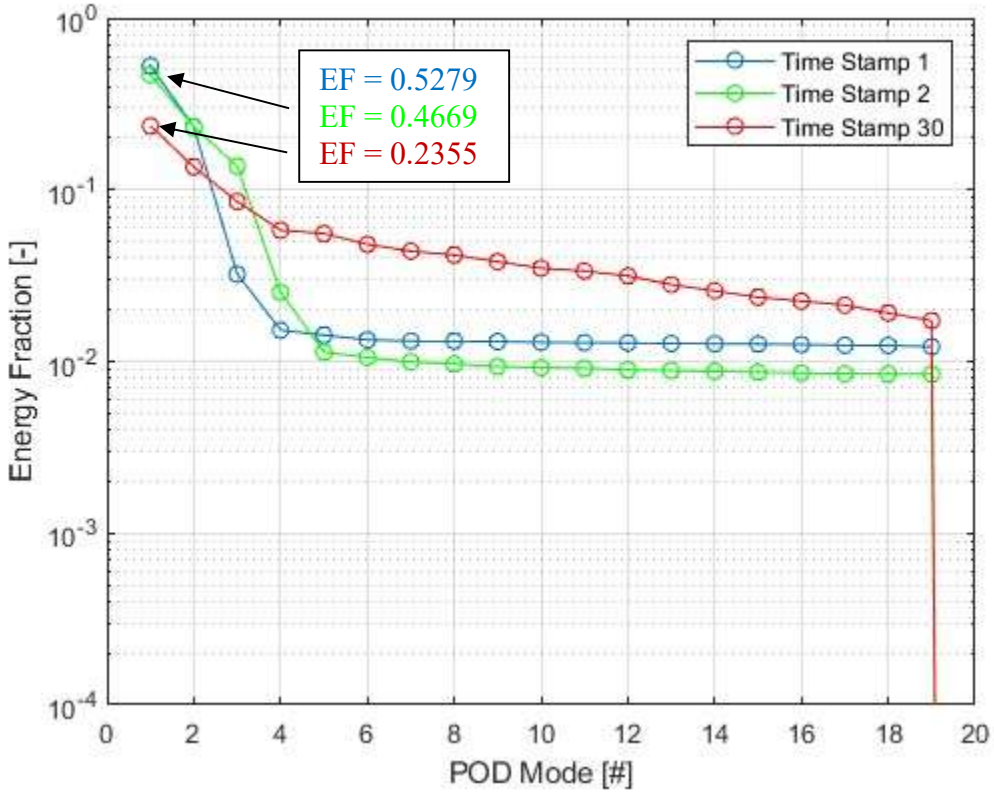



Figure 2.5 – Energy Fraction for SVD with Economy-size Decomposition

Even though this third approach and the second approach both utilize the MATLAB SVD function, the magnitudes are still double for the SVD with the correlation matrix approach. With this third approach the data is not centered by the mean, normalized, or standardized since the purpose of the SVD economy-size decomposition is to remove any extra rows or columns of zeros from the diagonal matrix of singular values, $S$. With the removal of these

zeros and columns, it can improve execution time and reduce storage requirements without comprising the accuracy of the decomposition. With the economy-size decomposition, it indicates that the magnitude in the energy fraction would not be present in the data like it is in the second approach.

Regardless of the energy fraction for each mode, the sum of energy fractions for the first 20 modes gives the value of 1, which confirms all data has been accounted for.

**Discussion**

With all three approaches under this research, it is found that there is a small amount of variability between each cycle and the first mode captures majority of the ensemble behavior. Figure 2.6 below displays the first time stamp from the above energy fraction graphs from the first 20 modes for each approach onto a single graph. With this visual, of all three, the eigenvalue problem and SVD without the correlation matrix overlap each other as they are identical. The study also observes the key differences of the SVD with correlation matrix approach. The main difference is the magnitude. The energy fraction of the first mode has a difference of 0.3014. What is unusual is the intersection between mode one and two. The energy fraction is the same for all three approaches around the middle of mode one and two, and then leads to the SVD with correlation matrix approach having a lower energy fraction than the other two approaches. The difference at mode two is 0.072, whereas the rest of the modes are close to double in magnitude, however, still following the same trend. The difference with these modes is assumed to be due to the MATLAB SVD function not requiring the use of a correlation matrix as other researchers and

mathematicians have found that the correlation matrix is performed within the function and the data does not need to be centered by the mean, normalized, or standardized.

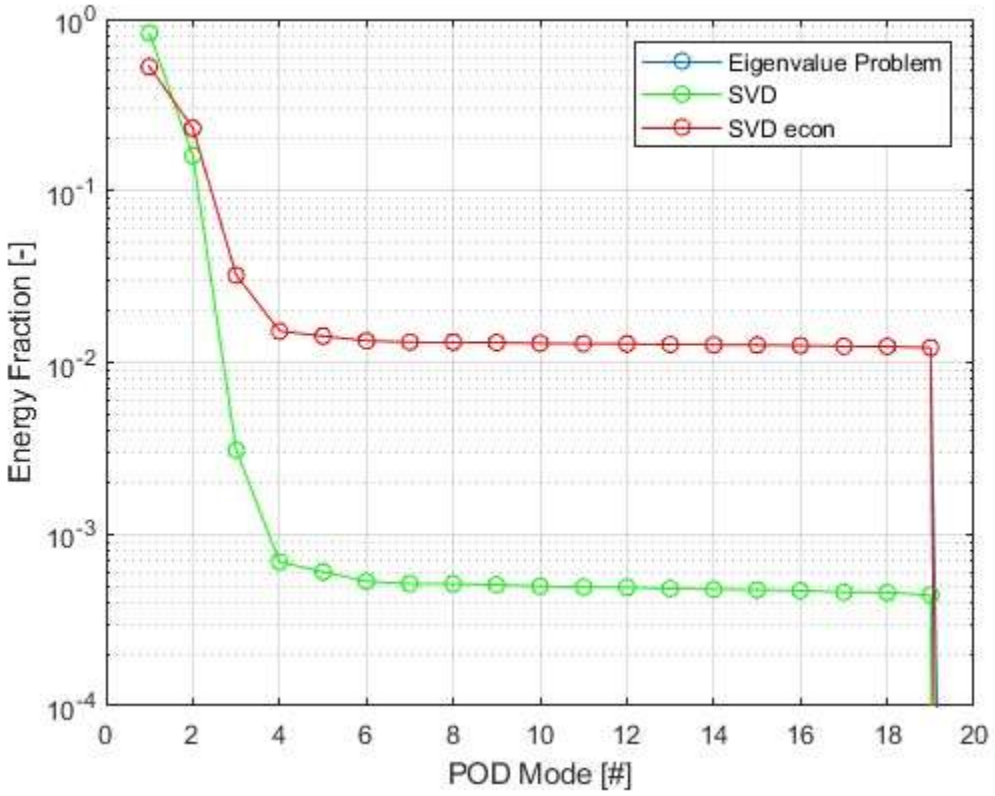



Figure 2.6 – Combined Energy Fraction Graph

Figure 2.6 also provides support on which approach should be used for the actual data analysis portion of this research. Ultimately, any approach could be used to analyze the variability amongst conditions, evaluate the quantitative differences in the spray patterns, and intensity in the variations. It is clear that the SVD is more economical when it comes to the number of lines within the code itself. The decision of which approach to use comes down to the dimensions of matrix $S$, depending on the size, solving the eigenvalue problem is often faster. This is caused by the SVD function still needing to compute the $n\ x\ n$ matrix $S'S$ to obtain its eigenvectors $V$ [5]. Therefore, for most applications in experimental or numerical fluid dynamics (where $n > m$), solving the eigenvalue problem is the method of

choice [5]. With the snapshot POD method, being the method of choice for this research and having an end goal of solving an optimization problem that gives the best representation of data, the economy-size SVD without the correlation matrix is chosen. This approach can handle mega pixel images and is one of the most useful matrix decompositions. It can also be used as a basis for principal component analysis for taking high dimensional data and trying to understand it in terms of its dominant patterns or correlations. When researching this approach, it was initially found in use by Dr. Brunton, a Mechanical Engineering professor at the University of Washington. Dr. Brunton provides a big picture overview of SVD and the use of an economy-size SVD in his videos. He shares examples of physical systems of snapshots that evolve in time into a data matrix and further shares that SVD is numerically robust and an efficient method of extracting patterns from data.

Another focus when studying the math under this research was the differences between $\lambda$ (lambda) and $\Sigma$ (sigma). Dr. Brunton describes the $S$ matrix as containing the singular values $\Sigma$ (ordered by importance diagonally) and that $\Sigma^2$ are the eigenvalues. Sirovich who developed the snapshot POD describes the eigenvalues as being $\lambda$. Another researcher and professor, Weiss, also describes that the matrix $S$ is the singular values of matrix $U$ and the eigenvalues are $\Sigma^2$. The last individual that discusses $\Sigma$ and $\lambda$ in his thesis is Luis G. Gutierrez Arsuaga who is another researcher that describes matrix $S$ containing the singular values of $\Sigma$ and $\lambda$ is $\Sigma^2$. With analyzing the research of four others, allowed for further interpretation of the differences between $\lambda$ and $\Sigma$. Each mention these symbols and what they represent slightly differently, however, it concludes the same meaning across each mention: $\lambda$ are the eigenvalues, which are $\Sigma^2$.

# CHAPTER 3

## Data Analysis and Interpretation

### Cycle-to-cycle Variability

The behavior of the spray plays a role in how the cycle variability is controlled. To identify coherent structures and cycle-to-cycle variability for extreme conditions in this experimental matrix the POD modes are analyzed under seven different conditions. The conditions are the injection pressure and chamber pressure ranging from 600 bar to 1500 bar and 1 bar to 20 bar, respectively. A quantitative analysis is performed to recognize processes of cycle-to-cycle variability and forced variability induced by experimental conditions.

### Injection Pressures of 600 bar

The first set that has been analyzed are the conditions of injection pressure 600 bar and chamber pressures of 1 bar and 20 bar. The first figure, Figure 3.1, displays the energy fraction for each condition. In both conditions, mode 1 is where the spray pattern intensity is the highest. 600 bar and 20 bar has an intensity of 23.5%, whereas 600 bar and 1 bar is 12.2%. 600 bar and 20 bar has a higher energy fraction for the first mode by 0.11, almost by half. This difference for the first mode could be linked to the higher chamber pressure of 20 bar rather than 1 bar. With increased chamber pressure, the spray area is expected to increase. What stands out among these two conditions is mode 3 where the energy fractions are nearly identical, which are then followed by lower energy fractions for the rest of the modes.

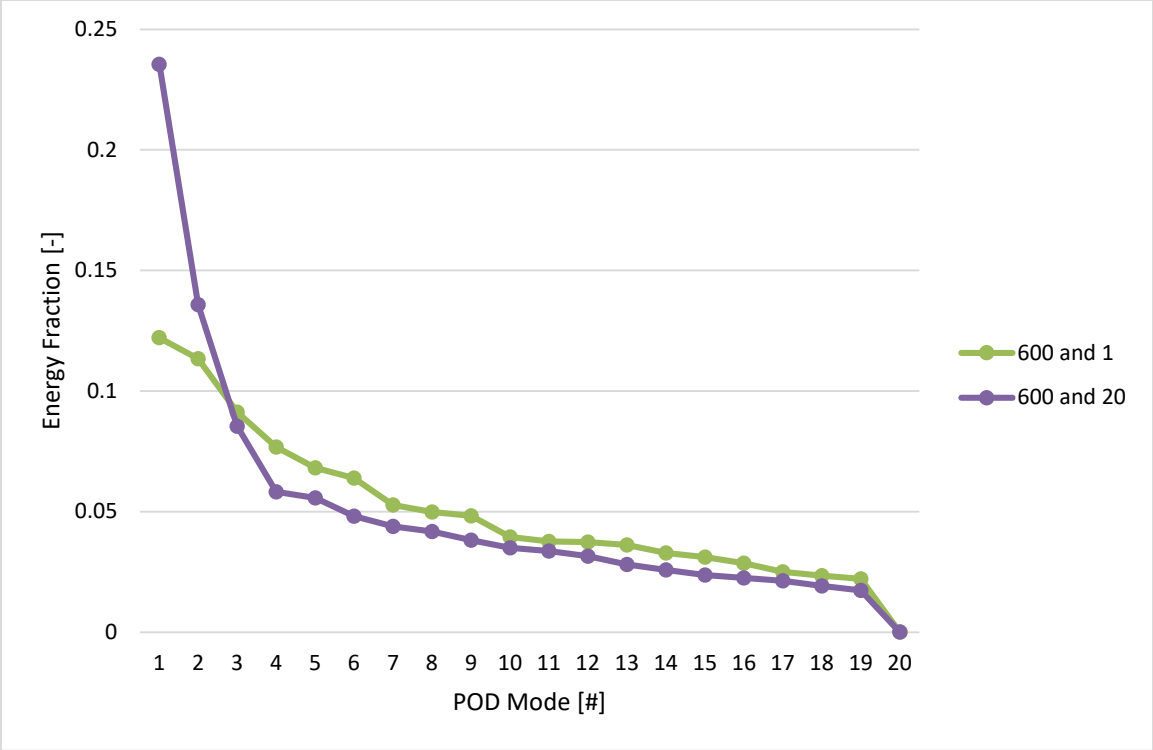



Figure 3.1 – Energy Fractions for Injection Pressures of 600 bar for Time Frame 30

Viewing the third mode of 600 bar and 1 bar, it has a slightly higher intensity present than what are in the 600 bar and 20 bar condition. As was described in the previous chapter, the input spray images are equal to the POD modes and the input images can be reconstructed with a lower-order estimation. The first three modes provide the greatest possible three-term approximation. Analyzing Figure 3.1 in conjunction with Figure 3.2, visually, it is evident that mode 1 has the highest energy fraction. The presence of the white color for the spray image shows the features that exist in the input image, those that are in black are the features that do not exist in the input image. Comparing mode 1 to modes 3 and 6, mode 1 for both conditions displays a greater presence of white, indicating that this mode has more features like the input image. Another visual realization is that the spatial droplet dispersion is one of the main differences between these two conditions. For the 600 bar and 1 bar condition, the same time frame as 600 bar and 20 bar (frame 30), penetrates past the frame

of the image. The droplets of the spray are dispersed at a much farther range for 600 bar and 1 bar, as is expected with the lower chamber pressure.

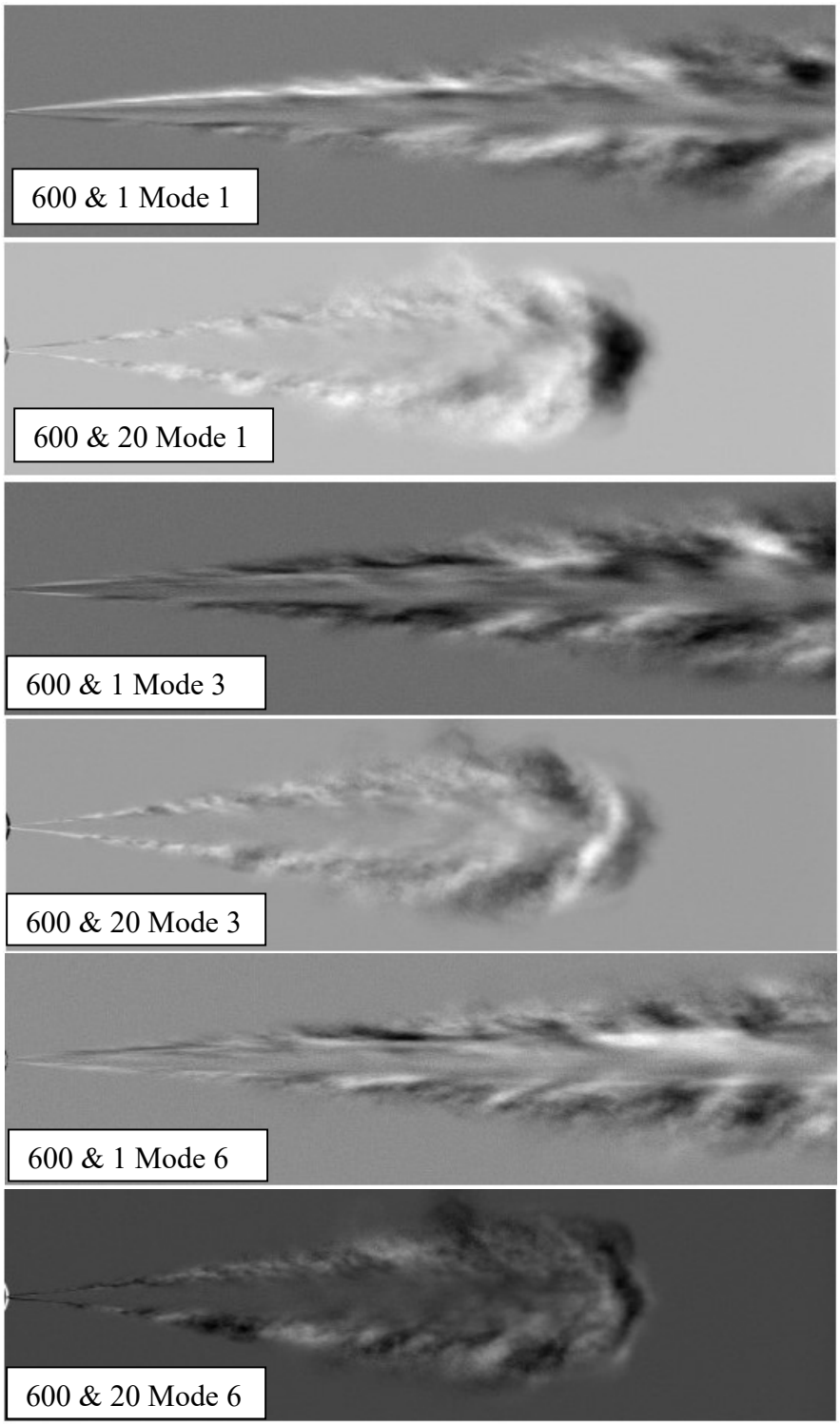



Figure 3.2 – Modes of 600 bar & 1 bar and 20 bar for Time Frame 30

With 600 bar and 20 bar, we see a small vortex has formed at the top of the spray area for mode 1. Since this vortex is displayed in white, it is also a present in the input images. For modes 3 and 6, there is a greater presence of black color and less features exhibited from the input images.

Coefficients are generated by the projection of each mode onto each snapshot [2]. Figures 3.3 and 3.4 include the coefficients of mode 1 for 20 spray images for the conditions being discussed, 600 bar and 1 bar and 600 bar and 20 bar. There is a fluctuation between positive and negative coefficients across the 20 spray images. In condition 600 bar and 1 bar, there are nine spray images that have negative coefficients, and the remaining are all positive indicating that more features from the original image are present.

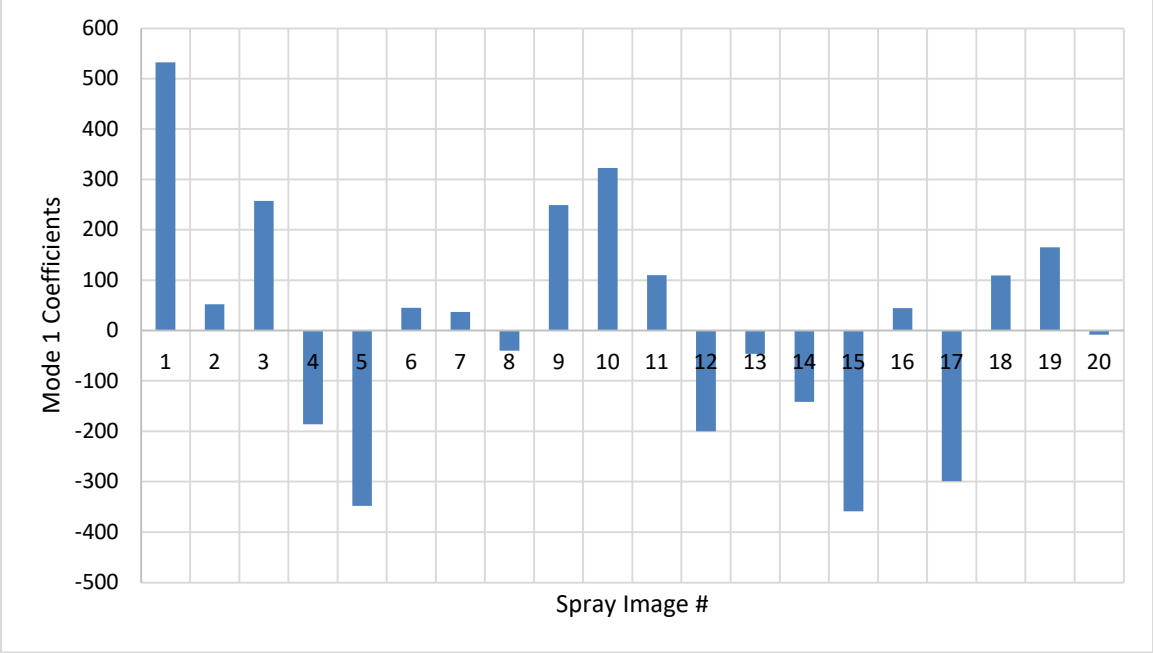



Figure 3.3 – Coefficients of Mode 1 for Condition 600 bar & 1 bar

Figure 3.4, condition 600 bar and 20 bar, on the other hand, has eleven spray images with negative coefficients. The more negative coefficients denotes that there are more features that do not exist in the input image. It is difficult to tell which condition is more like the

input image with only the energy fraction data and visuals of the modes. With the analysis of the first mode's coefficients for the spray images, it aids in discovering which condition exhibits more features from the input image. The mode 1 coefficients for these two conditions do not have a similar trend. With the first spray image, it is distinct that 600 bar and 1 bar has a positive coefficient of 532, whereas the 600 bar and 20 bar first spray image is a negative coefficient of 977, almost double of what 600 bar and 1 bar is, but in the opposite direction.

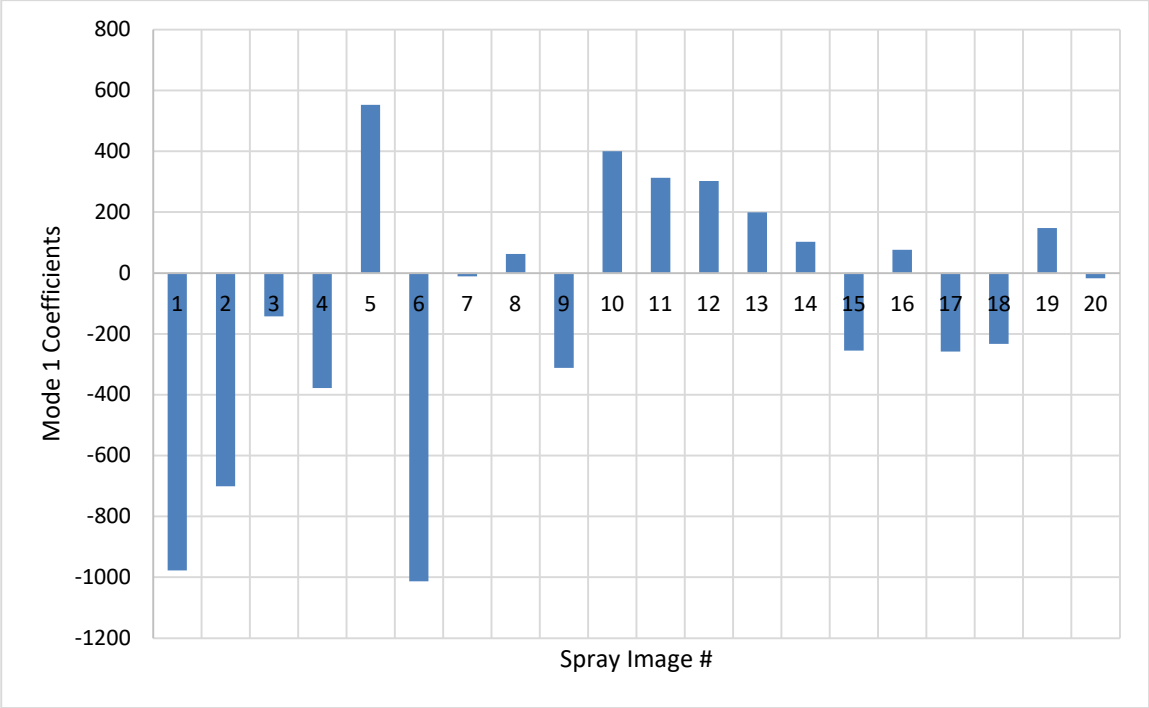



Figure 3.4 – Coefficients of Mode 1 for Condition 600 bar & 20 bar

The above analysis of the coefficients has only been performed for the conditions of 600 bar and 1 bar and 600 bar and 20 bar. The rest of the CCV analysis focuses on the energy fractions and modes for the remaining five conditions.

**Chamber Pressures of 1 bar**

The three conditions that were analyzed next under Figure 3.5 are that of chamber pressure 1 bar and injection pressures of 600 bar, 900 bar, and 1500 bar. The 1500 bar and 1 bar

condition has the highest energy fraction for the first mode of 21.8%, followed by 900 bar and 1 bar with 16.9%, and 600 bar and 1 bar with 12.2%. The higher the injection pressure, the higher the energy fraction these conditions have for the first mode.

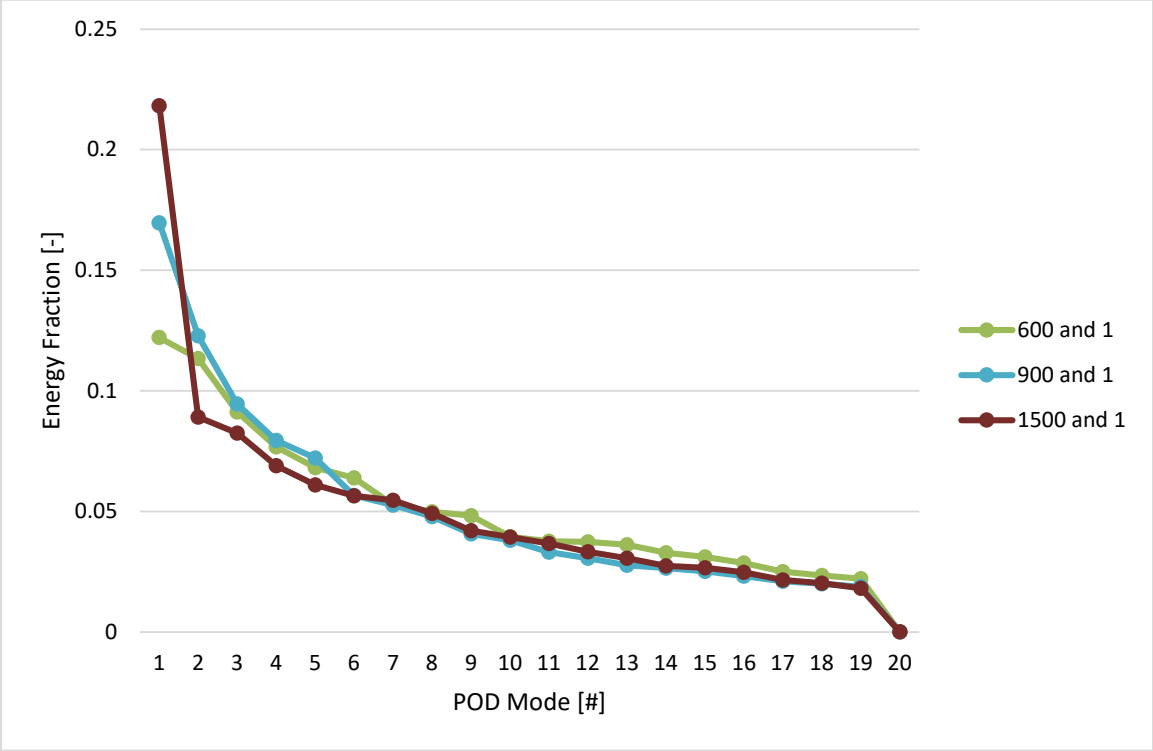



Figure 3.5 – Energy Fractions for Chamber Pressures of 1 bar for Time Frame 30

High injection pressure results with proficient fuel atomization and mixing, which created a more homogeneous charge that mitigates the formation of particulates [19]. This is what is noticed in the high injection pressure of 1500 bar. The range and width of the particulates is larger than that of the two other conditions. In Figure 3.6, the difference in the disbursement of particulates for 600 bar and 1 bar and 1500 bar and 1 bar is more extreme towards the right of the image. 600 bar and 1 bar presents a thinner width of particulates at the end of the right side of the frame than 1500 bar and 1 bar.

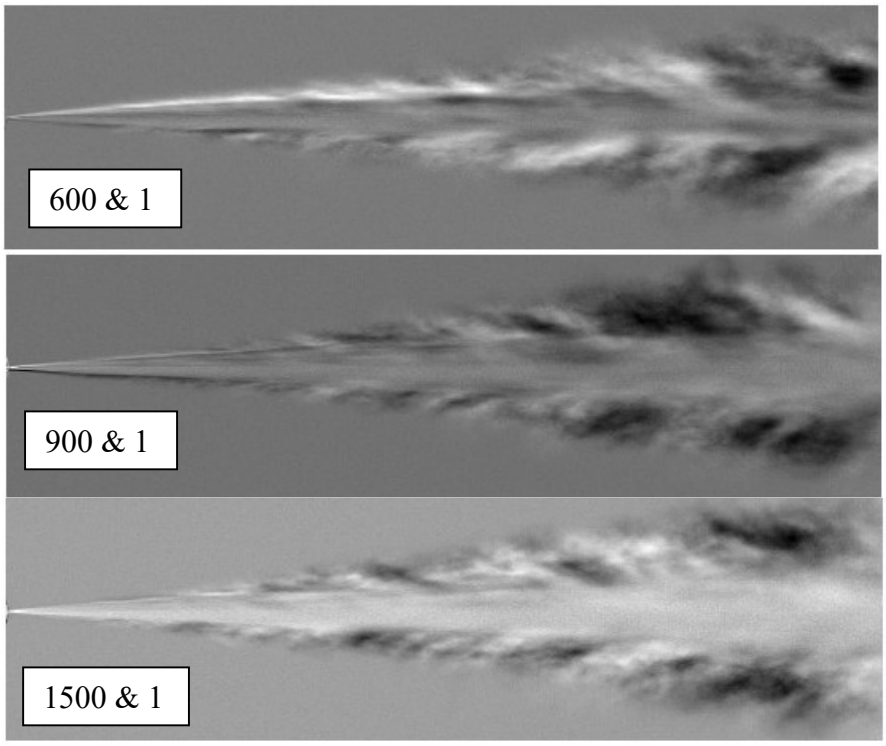



Figure 3.6 – First Mode of 600 bar, 900 bar, and 1500 bar and 1 bar for Time Frame 30

Like the images of the modes in Figure 3.2, Figure 3.6 also displays the white and black colors, indicating what features are present in the input images. Another observation that is made in the above figure is spray-induced turbulence. The fuel flow in the injector provides this spray turbulence, which helps the way the spray is distributed. High injection pressures that have high velocities produce more turbulence, which in return gives off an improved mixing between the fuel and air.

Analyzing Figures 3.5 and 3.6 together, the results indicate that the first mode is higher for the highest injection pressure, indicating that the morphology of the spray is more consistent and lower CCV is related with higher injection pressures. As the injection pressure decreases, the energy of the first mode decreases as we can see in the 900 bar and 600 bar condition in Figure 3.5, which here indicates that the differences in the spray

distribution from each cycle are starting to be much more complex and substantial, and therefore, will necessitate higher modes to determine the CCV.

### Injection Pressures of 1500 bar

The last two conditions that were analyzed are 1500 bar and 1 bar and 1500 bar and 20 bar. From the previous analysis comparing 600 bar, 900 bar, and 1500 bar and 1 bar conditions, it is known that the high injection pressure is expected to have a higher energy fraction. Unlike the comparison between the two 600 bar conditions, here the two 1500 bar conditions have the same energy fraction for mode 1 of 21.8%. The first mode shows the most statistically significant spatial differences between the cycles, therefore the spatial differences are the same for this mode for both conditions. However, 1500 bar and 1 bar drops significantly for mode 2 to 8.9%, whereas, 1500 bar and 20 bar had a slight decrease to 16.2%. The differences in energy fractions for mode 2 is likely linked to the difference in chamber pressure. With the higher chamber pressure of 20 bar, it is revealed that any aerodynamic forces that are acting on the spray droplets decrease the spatial differences. With the lower chamber pressure of 1 bar, there is less prevention of droplet movement and therefore, an increased variability between modes 1 and 2. By mode 3, the energy fractions become more consistent between the two conditions in a decreasing pattern.

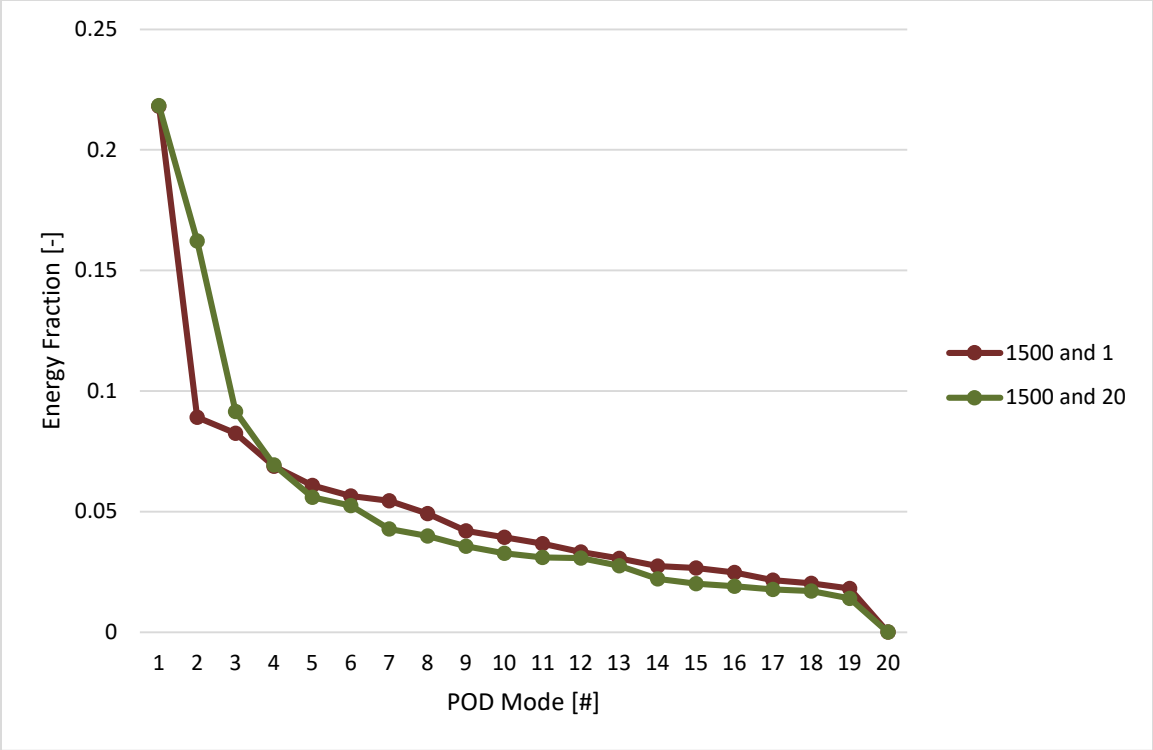



Figure 3.7 – Energy Fractions for Injection Pressures of 1500 bar for Time Frame 30

Interpreting the results in Figure 3.7 and 3.8 together, mode 1 shows the highest intensity. There are a lot of white areas present in both modes for Figure 3.8, again indicating features that are present in the input images. With the low chamber pressure of 1 bar, the spray penetrates past the frame of the image, excluding the tip of the spray for the analysis. The primary break-up and secondary break-up of the chamber pressure of 1 bar is still present for analysis. There are some similarities that are seen between both conditions in the first and second break-up periods. There is a pattern between black and white regions at the top and bottom portions of the spray. Some features along this path are present in the input images and some are not. What is most notable between the first modes of these conditions is the two black areas at the top and bottom of condition 1500 bar and 1 bar and not present in the 1500 bar and 20 bar condition. These are circled in red on the figure. The lower chamber pressure played a role on how quickly the spray was able to penetrate, leaving the

frame of the camera. The higher chamber pressure allowed for the spray droplets to decrease in penetration and remain in the camera's frame.

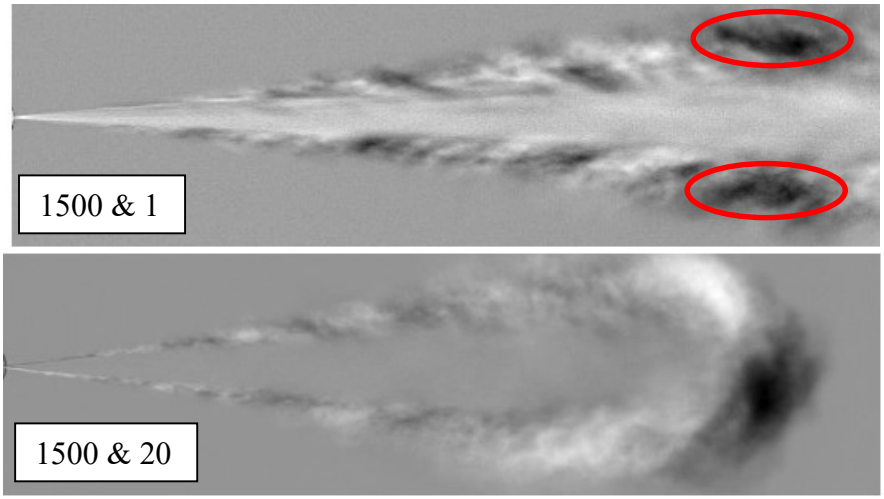



Figure 3.8 – First Mode of 1500 bar & 1 bar and 20

**Mode 1 vs. Time for Injection Pressures of 600 bar**

For each of the three analyzed cases above, the energy fractions of the first mode against time were analyzed. Figure 3.9 focuses on the first case of comparing conditions 600 bar and 1 bar and 600 bar and 20 bar. At the SOI up until around 0.072ms, both conditions follow the same trend. 600 bar and 1 bar begins with a slightly higher intensity at the SOI of 55.9% and 600 bar and 20 bar is 52.8%. This is followed by a quick decrease and then increase up to 70% for both conditions at 0.072ms. After 0.072ms, there is a significant decrease in the energy fraction for 600 bar and 20 bar, the decrease for 600 bar and 1 bar is more gradual. Since the chamber pressure is higher for 600 bar and 20 bar, this played a role in the development of the energy fraction for the first mode over time. The results here indicate that the image intensity from all the input images that are being captured are the highest 0.072ms ASOI and that intensity decreases over time. The energy fraction between the two conditions meets again at 0.159ms where now the 600 bar and 20 bar condition has

a higher intensity at 31.5% and 600 bar and 1 bar is at 29.6%. The higher chamber pressure of 20 reveals that a steep decline in intensity was needed prior to a stabilization that occurred after 0.159ms. As was previously discussed in the analysis under section 3.1.1, a higher chamber pressure relates to increased aerodynamic forces that act on the particulates of the spray, which in turn intensify the interaction between the air and liquid. Over time, the particulates break down into smaller particulates, and this is where we see less intensity.

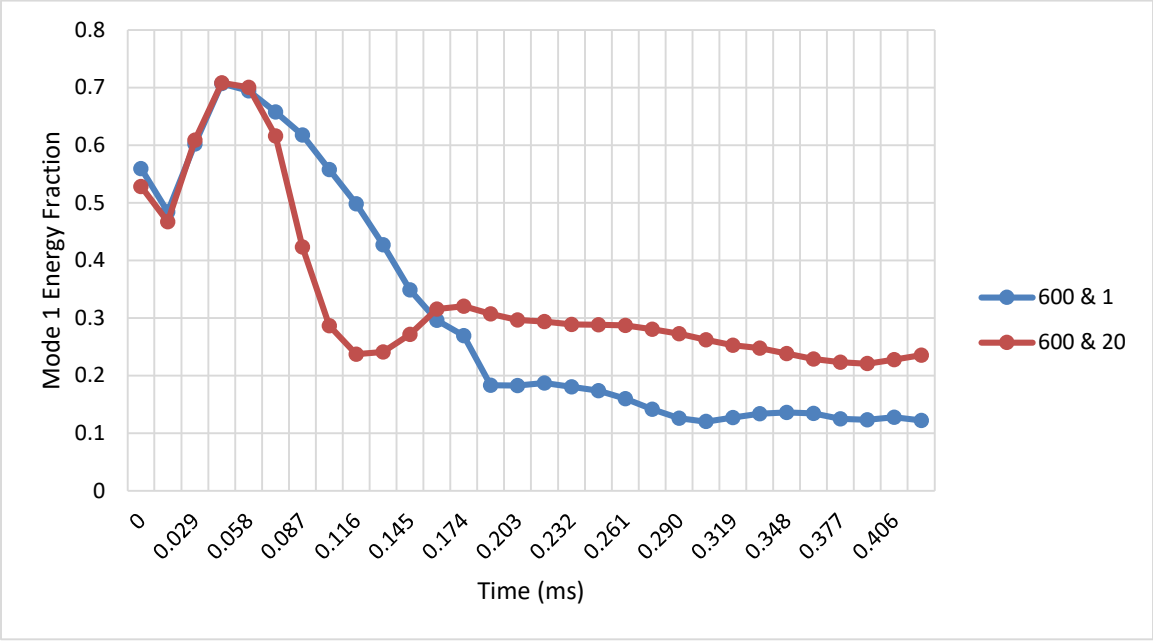



Figure 3.9 – Mode 1 vs. Time for Injection Pressure of 600 bar

**Mode 1 vs. Time for Chamber Pressures of 1 bar**

Figure 3.10 analyzes all three chamber pressures of 1 bar that were analyzed in section 3.1.2. Unlike the previous analysis for Figure 3.9, this case looks at three different injection pressures, all with a low chamber pressure of 1 bar. The higher two injection pressures of 900 bar and 1500 bar have a higher intensity at the SOI, whereas the 600 bar intensity at the SOI is not the highest throughout the time period. The 1500 bar injection pressure has the highest energy fraction of 91% at the SOI, followed by 900 bar with an energy fraction

of 85.2%, and lastly 600 bar with the lowest energy fraction of 55.9%. The energy fraction for 600 bar and 1 bar is not at its highest point until 0.043ms ASOI, where it is at 70%.

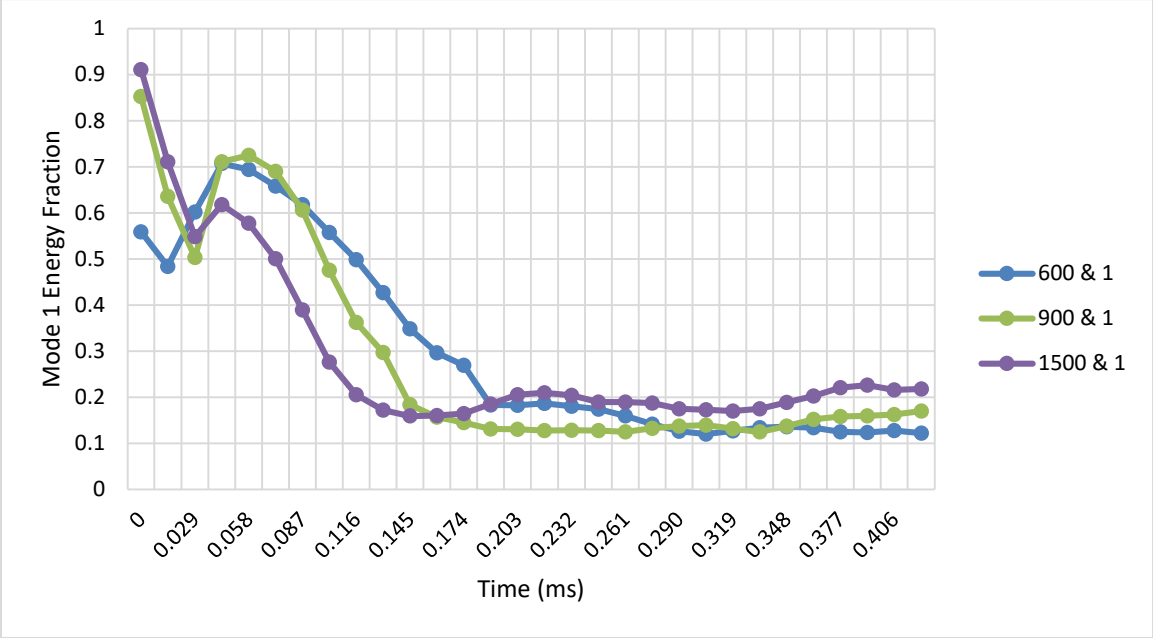



Figure 3.10 – Mode 1 vs. Time for Chamber Pressures of 1 bar

All three of these conditions have a similar trend over the time period shown. A decrease is seen right ASOI followed with an increase up to around 0.058ms, and then another decrease taking place to 0.174ms. After the last decrease in intensities, there is a stable trend until the end of time.

**Mode 1 vs. Time for Injection Pressures of 1500 bar**

The last case where the energy fractions of the first mode are analyzed against time is for the two conditions with the highest injection pressure of 1500 bar, 1500 bar and 1 bar and 1500 bar and 20 bar. Like the previous case, there is a decrease followed by a slight increase, and then another decrease until more stability is reached around 0.116ms. In section 3.1.4, the results indicated a higher energy fraction for 600 bar and 1 bar at the SOI. Here the same trend is seen for the lower chamber pressure, where 1500 bar and 1 bar has

a higher energy fraction that 1500 bar and 20 bar at the SOI. 1500 bar and 1 bar is at 91%, whereas 1500 bar and 20 bar is at 87%. Prior to the increase, both conditions have a drop in intensity by 0.029ms and then increase by 0.043ms ASOI.

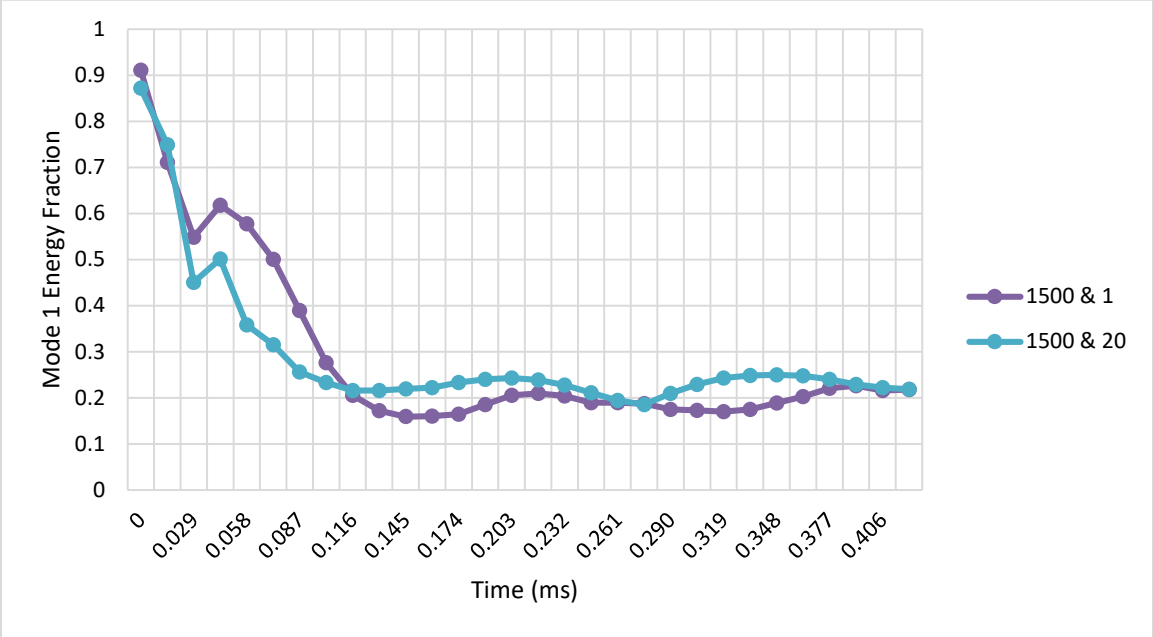



Figure 3.11 - Mode 1 vs. Time for Injection Pressure of 1500 bar

After 0.043ms is when the next decrease occurs followed by stabilization after the overlap between the two conditions at 0.116ms.

**Discussion**

The cycle-to-cycle variability analysis provided a depth of insight into the use of POD. Seven different conditions were able to be analyzed and interpreted by comparing energy fractions, modes, coefficients, and the coefficients of the first mode over time. In the first section, 3.1.1, where the two conditions of injection pressure 600 bar were analyzed, the results provided a conclusion that 600 bar and 20 bar has a higher energy fraction for the first mode by 0.11, almost by half. This difference for the first mode is suspected to be linked to the higher chamber pressure of 20 bar rather than 1 bar. With

increased chamber pressure, the spray area is expected to increase. The comparison of modes and coefficients between these two conditions further confirmed that an increased chamber pressure would provide a higher intensity. When three different injection pressures were looked at for the same chamber pressure of 1, it was identified that the higher the injection pressure, the higher the energy fraction these conditions had for the first mode. This scenario also showed the range and width of the particulates is larger for the higher injection pressure of 1500 bar than that of the two other conditions (600 bar and 900 bar). Another observation that was made for this same case is spray-induced turbulence. The fuel flow in the injector provides this spray turbulence, which helps the way the spray is distributed. High injection pressures that have high velocities produce more turbulence, which was seen in the 1500 bar condition. This then gives off an improved mixing between the fuel and air and the particulates are seen to cover more of the camera's frame than in the other two conditions with a lower injection pressure. Under the last case, the two highest injection pressures are interpreted against each other, with each having a different chamber pressure. The effects of the higher chamber pressure of 20 bar exposed that any aerodynamic forces that are acting on the spray droplets decrease the spatial differences. With the lower chamber pressure of 1 bar, there is less prevention of droplet movement and therefore, increased the variability between modes 1 and 2.

In sections 3.1.4 to 3.1.6 the results indicate that the higher the injection pressure, the higher the intensity is at the SOI, which confirms what has been discussed in the first three sections under 3.1. As time progresses the intensity decreases and then stabilizes. The higher chamber pressure leads to a more drastic decrease ASOI. The lower chamber pressure has a higher energy fraction at the SOI.

# CHAPTER 4

## Conclusion and Recommendations for Future Work

### Conclusions

The objective of this research was to evaluate different approaches to snapshot POD and find ways to compare them quantitatively. These approaches are the eigenvalue problem, SVD with a correlation matrix, and SVD using the economy size decomposition. Variability is studied between repetitions of the same condition i.e., cycle-to-cycle variability, and among different operating conditions i.e., injection pressure and chamber pressure. This research began with analyzing three different methods to approach snapshot POD. The analysis consisted of comparing the energy fractions between each method. The energy fractions of the eigenvalue method and the SVD econ method returned the same results for the energy fraction, whereas SVD with the use of a correlation matrix differed. All three methods subtracted the ensemble mean from the data matrix, which to this research meant that the first mode of the data would be interpreted as the structure that has the higher variance. Therefore, the first mode is a representation of the most statistically significant spatial differences between the cycles. Any method could have been chosen to move forward with analyzing the cycle-to-cycle variability amongst conditions. Ultimately, the SVD econ method was selected as it can handle mega pixel images and is one of the most useful matrix decompositions. It can also be used as a basis for principal component analysis for taking high dimensional data and trying to understand it in terms of its dominant patterns or correlations. The SVD econ method was able to provide results on cycle-to-cycle variability amongst seven selected conditions. Key conclusions, outcomes, and contributions of this research include the following:

- The eigenvalue problem, SVD with the use of a correlation matrix, or SVD econ could all be used to analyze the variability amongst conditions and evaluate the quantitative differences in the spray patterns, and intensity in the variations, however, it is clear that the SVD is more economical when it comes to the number of lines within the code itself.
- With increased chamber pressure, the spray area is expected to increase. The comparison of modes and coefficients between conditions of different chamber pressure indicated that an increased chamber pressure would provide a higher intensity.
- When analyzing conditions of high injection pressures such as 1500, it was observed that high injection pressures that have high velocities produce more turbulence giving off an improved mixing between the fuel and air. This results in the particulates of the spray being seen to cover more of the camera's frame than in the other two conditions with a lower injection pressure, leading to higher energy fractions.
- The results generated for the energy fractions against time, exhibited that the higher the injection pressure, the higher the intensity is at the SOI. As time progresses the intensity decreases and then stabilizes. The higher chamber pressure leads to a more drastic decrease ASOI. The lower chamber pressure has a higher energy fraction at the SOI.

The work shared in this thesis provides expansions and intuitions on valuable impacts to high-pressure gasoline sprays for internal combustion engines, specifically that of particulate formation across cycle-to-cycle variability. Even though this work focused

on the data analysis technique of POD, other methods could be used and this work could be expanded upon to analyze additional aspects of the spray and injector.

**Recommendations for Future Work**

The work described within this thesis analyzed three different approaches to snapshot POD, however, only one was selected to move forward with for data analysis and interpretation. Future work could consider including all three approaches into the data analysis for further insights into any differences as well as interpreting space-time POD. Also, the ensemble mean was subtracted from the data matrix. A comparison to the ensemble mean not being subtracted would help to provide awareness of the useful features that are given from each effect and a description for the average spray structure for the first mode.

The experiment that was performed for the analysis portion of this work included the use of three different injectors. The injector that was focused on for this analysis is Injector 1, which is a single hole centered injector. Injectors 2 and 3 are both double hole injectors and have different hole sizes than that of Injector 1. Performing POD on all three injector types would provide an additional contribution to this research. Looking into other variability like internal nozzle geometry would allow for more discussion and conclusions.

Lastly, there are several features of the spray images that were not focused on such as the spray contour, axis, diameter, penetration, droplet size and velocity, spatial distribution, and potential cavitation effects. Additional features and spray characteristics could be added to this list. Ultimately, inspecting more features of the spray for the different conditions would give meaningful contributions to this research.

REFERENCES

[1] A. Chatterjee, "An Introduction to the Proper Orthogonal Decomposition," *Current Science, Vol. 78 No. 7,* pp. 808-817, 2000.

[2] H. Chen, D. L. Hung, M. Xu and J. Zhong, "Analyzing the Cycle-to-Cycle Variations of Pulsing Spray Characteristics by Means of the Proper Orthogonal Decomposition," *Atomization and Sprays,* vol. 23, pp. 623-641, 2013.

[3] C. Rowley, "Model Reduction for Fluids, Using Balanced Proper Orthogonal Decomposition," *International Journal of Bifurcation and Chaos,* vol. 15, no. 3, pp. 997-1013, 2004.

[4] T. L. F. F. Ang, M. P. F. Choolani, K. C. F. M. See and K. K. F. F. Poh, "The rise of artificial intelligence: addressing the impact of large language models such as ChatGPT on scientific publications," *Singapore Medical Journal,* vol. 64, no. 4, pp. 219-221, 2023.

[5] J. Weiss, "A Tutorial on the Proper Orthogonal Decomposition," in *2019 AIAA Aviation Forum*, Dallas, 2019.

[6] H. Chen, D. L. S. Hung, M. Xu, H. Zhuang and J. Yang, "Proper orthogonal decomposition analysis of fuel spray structure variation in a spark-ignition direct-injection optical engine," *Exp Fluids,* vol. 55, no. 1703, pp. 1-12, 2014.

[7] H. Chen, D. L. Reuss, D. L. Hung and V. Sick, "A practical guide for using proper orthogonal decomposition in engine research," *International Journal of Engine Research,* vol. 14, no. 4, pp. 307-319, 2012.

[8] T. Colonius and M. Daleh, "POD analysis of sound generation by a turbulent jet," in *AIAA Paper 2002-2007*, 2002.

[9] L. David, L. Thomas and R. Vernet, "Analysis and reconstruction of a pulsed jet in crossflow by multi-plane snapshot POD," *Experiments in Fluids,* vol. 47, pp. 707-720, 2009.

[10] E. Shlizerman, E. Ding, M. O. Williams and J. N. Kutz, "The Proper Orthogonal Decomposition for Dimensionality Reduction in Mode-Locked Lasers and Optical Systems," University of Washington, Seattle.

[11] K. Baker, "Singular Value Decomposition Tutorial," Ohio State University, Columbus, 2005.

[12] B. C. Moore, "Principle Component Analysis in Linear Systems: Controllability, Observability, and Model Reduction," *IEEE Transactions on Automatic Control,* vol. 26, no. 1, pp. 17-32, 1981.

[13] S. Lall, J. E. Marsden and S. Glavaski, "A subspace approach to balanced truncation for model reduction of nonlinear control systems," *International Journal of Robust and Nonlinear Control,* vol. 12, pp. 519-535, 2002.

[14] B. Van Oudheusden, F. Scarano, N. Van Hinsberg and D. Watt, "Phase-resolved characterization of vortex shedding in the near wake of a square-section cylinder at incidence," *Experiments in Fluids,* vol. 39, no. 1, pp. 86-98, 2005.

[15] L. Sirovich, "Turbulence and the dynamics of coherent structures. I. Coherent structures," *Quarterly of Applied Mathematics,* vol. 45, no. 3, pp. 561-571, 1987.

[16] M. Medina, "High-Speed Imaging Studies of Gasoline Fuel Sprays at Fuel Injection Pressures from 300 to 1500 bar," SAE International, Ann Arbor, 2018.

[17] M. Medina and Y. Zhou, "High-Speed Imaging Study on the Effects of Internal Geometry on High-Pressure Gasoline Sprays," SAE International, Ann Arbor, 2020.

[18] H. Chen, D. L. Reuss and V. Sick, "On the use and interpretation of proper orthogonal decomposition of in-cylinder engine flows," *Measurement Science and Technology,* vol. 23, pp. 1-14, 2012.

[19] L. G. Gutierrez Arsuaga, "Advanced Diagnostics for Spray Behavior; Fuel Impingement, and Soot Processes in Direct Injection Spark Ignition Engines," University of Michigan, Ann Arbor, 2019.

[20] S. Lall, J. E. Marsden and S. Glavaski, "Empirical model reduction of controlled nonlinear systems," *IFAC Proceedings Volumes,* vol. 32, no. 2, pp. 2598-2603, 1999.